Analysis of hybrid nanoparticles shape factor and thermal radiation effect on solidification in latent energy storage in a triplex chamber

OMID MANSOURSAMAII[1], JAHANFAR KHALEGHINIA[1,*], MORTEZA MOHAMMADI[1], BAHRAM JAFARI[2] and RAMEZAN REZAEYAN[3]

[1]Department of Mechanical Engineering, Nour Branch, Islamic Azad University, Nour, Iran
[2]Department of Engineering Modern Technologies, Amol University of Special Modern Technologies (AUSMT), Amol, Iran
[3]Department of Statistics and Mathematics, Nour Branch, Islamic Azad University, Nour, Iran
*Corresponding author. E-mail: j.khaleghinia@gmail.com

Abstract.   Researchers have made many efforts to store energy in forms that can be turned into required forms. Energy storage minimises the gap between supply and demand for energy while increasing energy systems' effectiveness and dependability. Latent heat storage (LHS) can be used to store energy efficiently. This article explores the numerical analysis of the solidification procedure for latent heat thermal energy storage (LHTES) in a triplex chamber. TiO_2–Al_2O_3 nanoparticles were used as hybrid nanoparticles and water was used as a phase change material (PCM). FlexPDE, a general-purpose scripted finite-element software, was used to discretise and solve the partial differential governing equations. The study investigated the impact of various factors on the contour of solid fraction, temperature distribution, average temperature, solid fraction diagram and the overall energy of the system. These factors encompassed the volume fraction of nanoparticles, the presence of fins, thermal radiation and the shape factor of nanoparticles. Moreover, the optimal values for the full solidification time (FST) were established using the response surface methodology (RSM). The findings indicate that full solidification time is optimised when the hybrid nanoparticle volume fraction is 0.048, thermal radiation is 0.777 and shape factor is 15.29.

1. Introduction

Thermal energy storage systems contribute highly in improving energy efficiency and enhancing energy systems' reliability while also helping balance the energy supply and demand. Zhao *et al* [1] assessed the melting and freezing phase change process by conducting some experiments. They used RT58 paraffin and metal waxes as phase change material (PCM) to enhance heat transfer. The test samples were heated electrically at a low level under constant flux conditions during the melting process. According to these researchers, adding metallic foam gives a 3–10 fold increase in the overall heat transfer coefficient. Rostamizadeh *et al* [2] employed an enthalpy-based mathematical model to examine how the thickness of the PCM impacts the temperature distribution and melting ratio. Results showed a linear relationship between the melting time and the PCM thickness. Thinner layers were found to improve the performance. Moradi *et al* [3] examined a solar air heater utilising paraffin as the phase changer. PCM under the absorber plate can enhance the system's thermal efficiency by generating one-third of the total thermal energy during the melting procedure. Also, the thermal performance of two different PCMs used in concrete walls was assessed by Saikia *et al* [4]. In this research, different geographical directions for the walls were also investigated. Zinc nitrate as a PCM showed improved thermal performance regarding its extended latent heating duration, resulting in reduced temperature fluctuations in all directions analysed.

In another study, the melting process between two oval cylinders was investigated numerically by Faghani *et al* [5]. In this research, the shapes of the shell and tube were considered circular or oval, nine different geometries were investigated and commercial material RT 25 was used as the PCM. Lin *et al* [6] conducted a laboratory investigation on an innovative latent heat thermal energy storage (LHTES). The analysis results revealed that the system released 6.3 MJ of energy at 4 kW and achieved a heat transfer coefficient of 25–70 W/K for flow rates of 100–5001/h, demonstrating its potential for efficient thermal energy storage and transfer.

Moreover, fins can be utilised to enhance heat transfer in PCM systems regarding these conductive heat transfer coefficient. Sciacovelli *et al* [7] suggested the use of tree-shaped fins to improve the tube LHTES and shell performance. They concluded that the optimum design of the fin is based on the operating time of the LHTES. Joybari *et al* [8] conducted a numerical study on the effects of using wide surfaces (longitudinal fins) on the material's melting and freezing process in the donor's phase alterations in a triplex heat exchanger. They concluded that a configuration with three hot tubes and a cold tube fin is compatible with natural convection heat transfer and has the best system performance. Liu *et al* [9] suggested a longitudinal triangular fin to improve heat transfer characteristics in a shell and tube LHTES device. Patel and Rathod [10] studied the freezing and melting procedure of the PCM numerically in a three-wall chamber for LHTES. The results showed that internal and combined vanes are equally effective during the melting process as they reduce 60% of the melting time. Kirincic *et al* [11] investigated the charge and discharge processes in an LHTES device. They found reductions of 52% and 43% in total melting time and total solidification time, respectively, in the system equipped with longitudinal fins compared to the plain tube configuration. In addition, Shafiq *et al* [12] studied the impact of various fin geometries numerically on enhancing the performance of a double-walled rectangular thermal energy storage unit. Yang *et al* [13] offered a creative method to design thermal energy storage by adding combined metal foam and fins to PCMs.

Thermal conductivity is a key feature in the thermal performance of the working fluid. Nanoparticles possess high conductivity coefficient compared to regular fluids, making them a significant characteristic of these materials. Hosseinizadeh *et al* [14] utilised a nanoenhanced PCM (NEPCM) in a spherical chamber to enhance heat transfer. The results revealed a reduction in the complete solidification time of the PCM-containing nanoparticles by increasing the volume fraction.

Furthermore, Wu *et al* [15] assessed the melting and solidification procedure of the PCM-containing
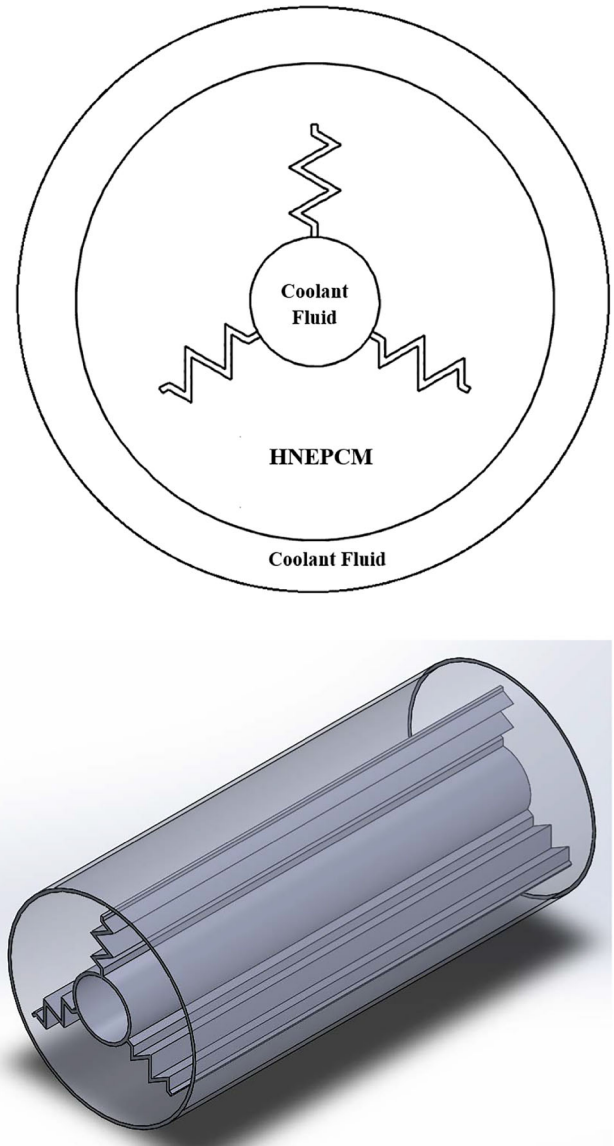

Figure 1. Views in two and three dimensions, as well as the study's boundary conditions.

nanoparticles. Based on the results, the maximum increase in thermal conductivity (18.1% in the liquid state and >14.2% in the solid state) occurs in copper/paraffin 2 wt.%. Sheikholeslami and Ghasemi [16] investigated the solidification process of PCM-containing nanoparticles by analysing the unsteady heat transfer under thermal radiation. They used water as the phase changer and copper oxide as nanoparticles. Khan *et al* [17] conducted a numerical study of the performance of a shell-and-tube heat exchanger, including PCMs and nanoparticles. According to their results, an increase in the volume concentration of nanoparticles leads to significant improvements in melting and solidification rates, conductive heat transfer and maximum

Table 1. The physical properties of water as PCM, hybrid nanoparticles and fin [28–30].

Property	PCM	Al_2O_3	TiO_2	Fin
ρ (kg/m^3)	997 (Liquid phase) 916 (Solid phase)	3970	4250	8960
C_p (J/kg K)	4184 (Liquid phase) 2030 (Solid phase)	765	686.2	385
k (w/mK)	0.6 (Liquid phase) 2.22 (Solid phase)	25	18	400
L_f (J/kg)	335,000	–	–	–
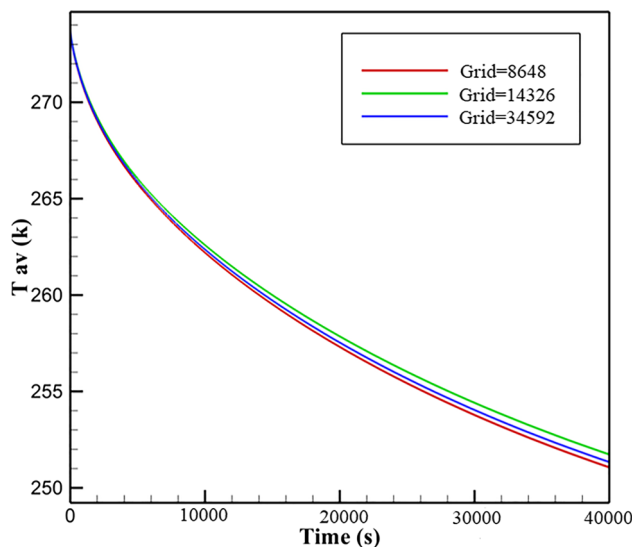
Figure 2. Analysis of grid independency.

Figure 3. View of grid quality.

2. Problem statement, numerical method and validation

Figure 1 presents the two-dimensional schematic of the geometry investigated for the LHTES system in this research. As can be seen, the chamber is designed such that the cooling fluid flows through both the central and outer layers to ensure effective cooling. In addition, the layer with HNEPCM is situated between the inner and outer layers, where the cooling fluid flows. The PCM temperature in the HNEPCM layer is maintained at 278 K, while the cooling fluid temperature is set at 240 K. TiO_2–Al_2O_3 hybrid nanoparticles and water (as the PCM) were used to enhance the speed of solidification inside the chamber. The thermophysical features of the fin, the HNEPCM and the PCM are provided in table 1 [28–30].

The summarised assumptions and boundary layer conditions are as follows:

1. The geometry is simulated in two dimensions.
2. The solidification process is unsteady.
3. The thermophysical characteristics of the fluid are considered to be time-dependent.

Also,

1. The initial temperature of the phase-changing nanofluid is 278 K.
2. The cooling fluid temperature is constant and equal to 240 K.
3. The outer surface of the chamber is adiabatic.
4. Different shapes of nanoparticles are considered (table 2) [28–30].

heat flux. Yadav *et al* [18] observed the enhanced performance of a solar thermal storage system via PCMs containing nanoparticles. Zadeh *et al* [19] conducted a numerical study on the heat transfer increment of a thermal energy storage system with latent heat by adding metal foam and nanoparticles. Also, they integrated Cu/GO nanoparticles and copper foam to enhance heat transfer properties. They found that using GO nanoparticles results in more favourable heat transfer properties than Cu nanoparticles (see [20–27] for more information on the effects of nanoparticles on heat transfer enhancement).

The present research delved into the influence of hybrid nanoparticles, the shape factor, extended surfaces and thermal radiation parameters on expediting PCM solidification within the triplex LHTES chamber. The objective of this study was to evaluate the impact of diminishing solidification time and augmenting discharged energy on the solidification process within the latent energy storage of a triplex chamber.
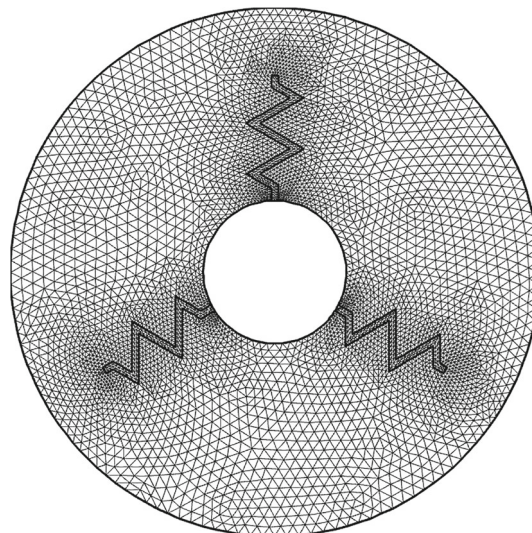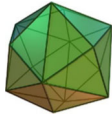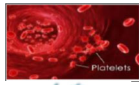
Table 2. Different shapes of nanoparticles [28–30].

Nanoparticles type	Shape	Shape factor
Hexahedron		3.7
Platelets		5.7
Lamina		16.1

The governing equations in the system are given as [14]

Continuity equation:

$$\frac{\partial u_i}{\partial x_i} = 0. \tag{1}$$

Momentum equation:

$$\frac{\partial u_i}{\partial t} + u_j \frac{\partial u_i}{\partial x_i}$$
$$= \frac{1}{\rho}\left(\mu_{\text{eff}} \nabla^2 u_i - \frac{\partial p}{\partial x_i} + \rho\beta_e(T - T_{\text{ref}})g_i\right), \tag{2}$$

where ρ is the density, t is related to time, β_e is the coefficient of thermal expansion, g_i represents the acceleration of gravity, μ denotes the dynamic viscosity of the fluid, p is the pressure and T_{ref} represents the reference temperature.

Energy equation:

$$(\rho C_p)_{hnf}\frac{dT}{dt} = \nabla(k_{knf} \nabla T) + L_{knf}\frac{dS}{dt} - \frac{\partial q_r}{\partial y},$$
$$q_r = -\frac{a\sigma_\varepsilon}{3\beta_R}\frac{\partial T}{\partial y},$$
$$T^4 = 4T_0^3 T - 3T_0^4, \tag{3}$$
$$Rd = \frac{a\sigma_\varepsilon T_0^3}{3\beta_R k_f},$$

where T denotes the temperature, C_p is the specific heat capacity, q_r is related to the radiation parameter, L_f is the latent heat of the solid–liquid phase change, k represents the conductive heat transfer coefficient and S is the solid fraction.

The energy equation in the solid part, including the chamber and fins, is as follows:

$$\rho C_p \frac{dT}{dt} = \nabla(k \nabla T). \tag{4}$$
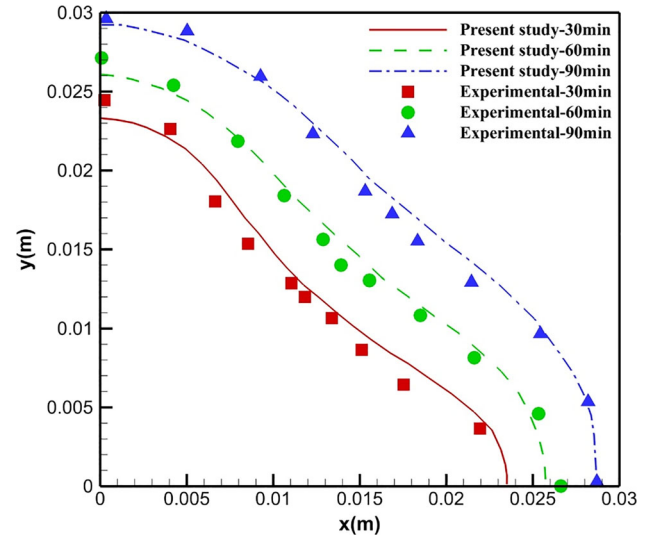
Figure 4. Validation of the current simulation with the experimental investigation of Ismaeil *et al* [34].

Solid fraction equation:

$$\begin{cases} S = \left(T_m + \dfrac{T_0}{2} - T\right)/T_0 \\ \qquad\qquad (T_m - T_0) < T < (T_m + T_0), \\ S = 1 \qquad\qquad T < (T_m - T_0), \\ S = 0 \qquad\qquad T > (T_m + T_0), \end{cases} \tag{5}$$

where S, T_m and T_0 stand for the solid fraction, melting temperature and melting interval, respectively, while T is the temperature.

The following expressions are used to analyse the thermophysical characteristics of HNEPCM [22,31,33]:

$$\rho_{hnf} = \rho_f(1 - \phi_2)\left[(1 - \phi_1) + \phi_1\left(\frac{\rho_{s1}}{\rho_f}\right)\right] + \phi_2\rho_{s2}, \tag{6}$$

$$(\rho C_p)_{hnf} = (\rho C_p)_f (1 - \phi_2)$$
$$\times \left[(1 - \phi_1) + \phi_1\frac{(\rho C_p)_{s1}}{(\rho C_p)_f}\right]$$
$$+ \phi_2(\rho C_p)) s2, \tag{7}$$

$$(\rho L_f)_{hnf} = (\rho L_f)_f(1 - \phi_2)(1 - \phi_1), \tag{8}$$

$$\frac{k_{hnf}}{k_{bf}} = \frac{k_{s2} + (sf - 1)k_{bf} - (sf - 1)\phi_2(k_{bf} - k_{s2})}{k_{s2} + (sf - 1)k_{bf} + \phi_2(k_{bf} - k_{s2})},$$
$$k_{bf} = k_f\frac{k_{s1} + (sf - 1)k_f - (sf - 1)\phi_1(k_f - k_{s1})}{k_{s1} + (sf - 1)k_f + \phi_1(k_f - k_{s1})}, \tag{9}$$

where C_p, ρ and L denote specific heat, density and latent heat, respectively, whereas the subscripts *bf*, *hnf*
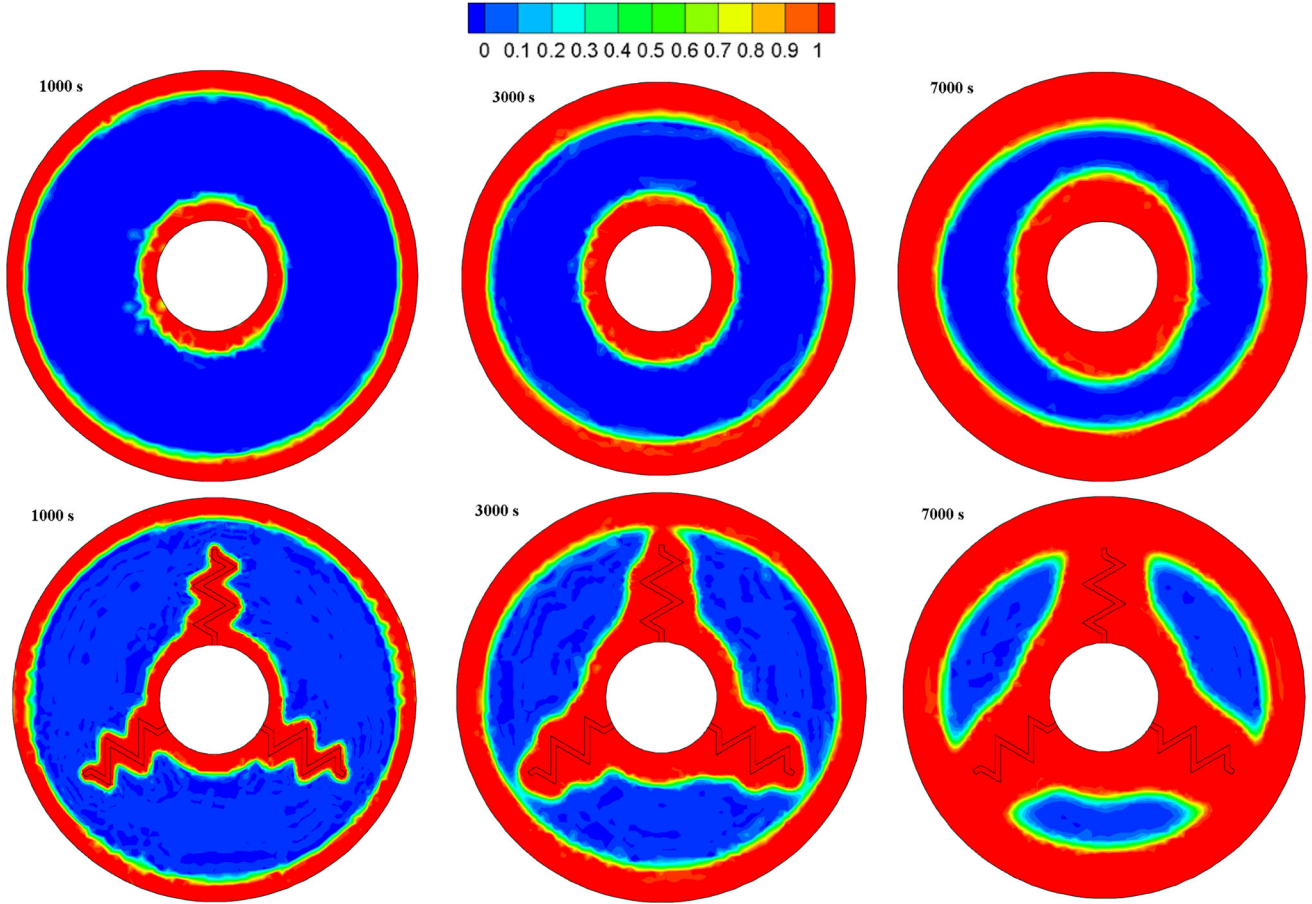
Figure 5. The comparison of solid fraction contour of the normal chamber and the finned chamber.

and f and s represent the base fluid, hybrid nanofluid, fluid and solid, respectively.

These relationships assist in determining specific heat, density and latent heat, each of which is demonstrated by C_p, ρ and L. Additionally, each linked subscript provided hnf, bf, f and s denotes a solid, base fluid, fluid, or hybrid nanofluid, respectively.

The quantity of two types of energy (i.e., latent and sensible) can be determined in this work as follows [31–33]:

$$E_{\text{sensible}} = mC_pT = \rho V C_p T \tag{10}$$

$$E_{\text{latent}} = m(1 - S)L_f = \rho V(1 - S)L_f. \tag{11}$$

The total quantity of energy within the computational domain can be calculated as

$$E_{\text{total}} = E_{\text{sensible}} + E_{\text{latent}}$$
$$= \rho \int (C_pT + (1 - S)L_f)\mathrm{d}V. \tag{12}$$

Besides, the average temperature of the PCM during the process can be measured as

$$T_{\text{ave}} = \frac{\int T\,\mathrm{d}A}{\int \mathrm{d}A}. \tag{13}$$

In this investigation, the simulation of the solid–liquid phase change process was conducted in detail using the Flex PDE open-source software. It is noteworthy that this software utilises the standard Galerkin finite-element method (GFEM) employing quadratic interpolation based on the finite-element approach. The solutions were computed in continuous spatial coordinates with the nodes' values at the grid cells' sides and corners. The Galerkin equations were formed and the definitions were replaced, followed by applying the integral and forming the coupling matrix by derivation with respect to the system variable. Finally, the equations were simultaneously solved using the conjugate gradient iteration method.

3. Grid independency check and validation

Grid independence is tested using three alternative grid sizes to simulate the problem. The impact of grid size has
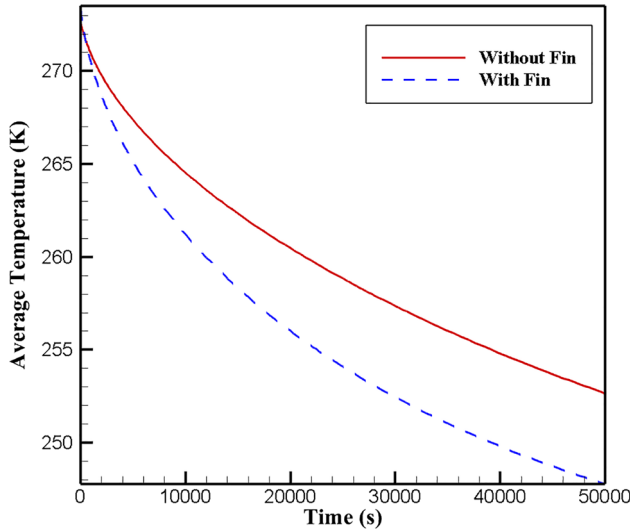
Figure 6. Temperature distribution diagram for modes with and without fins.
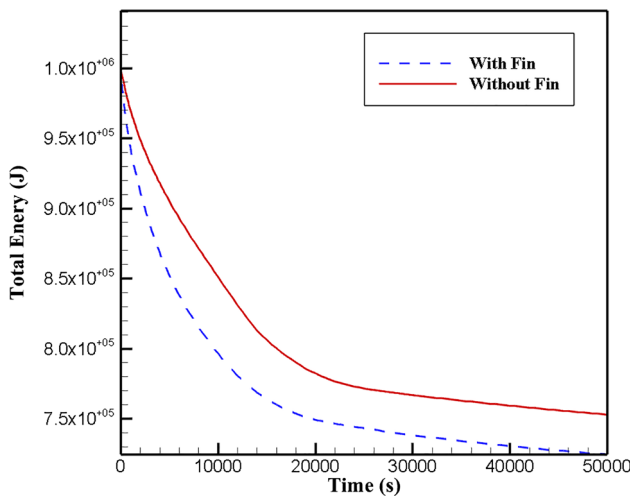

Figure 7. Total energy distribution diagram for two modes with and without fins.

been investigated on the average temperature of PC-M. According to figure 2, there is no considerable difference between the 14326 and 34592 grid numbers. A grid size of 14326 was employed in the following to save both time and money. Figure 3 illustrates the mesh's level of quality.

The reliability of the current study was verified using GFEM by replicating a former experiment conducted by Ismail *et al* [34]. Figure 4 compares the outcomes of the present methodology and the experimental study. The results show excellent agreement between the findings of both studies, with an error of no more than 5% at any stage of the process. This agreement confirms the authenticity and reliability of the current research. Ismail *et al* conducted a numerical and experimental
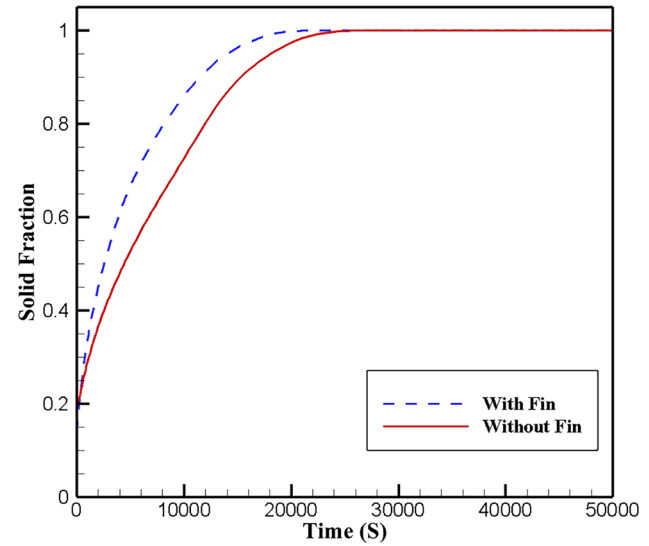

Figure 8. The comparison of solid fraction contour of the normal chamber and the finned chamber.

analysis on finned tubes with the goal of employing them in TESS. The model is based on the pure conduction mechanism of heat transfer, the enthalpy formulation technique and the control volume method.

4. Results and discussion

In this section, we analyse the influence of various factors on the solidification process. Specifically, we investigate the impact of fins, the volume fraction of HNEPCM, radiation parameter and different shapes of HNEPCM. Each aspect will be evaluated separately, with different shapes and configurations presented in each section to explore the effects of each parameter.

4.1 *Analysing the impact of using fins*

Figure 5 illustrates the mass fraction contour for two scenarios (i.e., one with a standard inner chamber and the other with a finned inner chamber) at various time intervals (1000, 3000 and 7000 s). The inclusion of fins improves the conductive heat transfer mechanism and accelerates the transfer of heat into the chamber's interior, thereby accelerating solidification inside the chamber. Figure 6 shows the temperature distribution for two scenarios: (1) with fins and (2) without fins. The mean temperature of the PCM is greater in the absence of fins than in the presence of fins. Additionally, when fins are employed, temperature variations are greater. The temperature difference of the PCM in the chamber is therefore improved by the inclusion of fins, increasing heat transfer. The total energy for
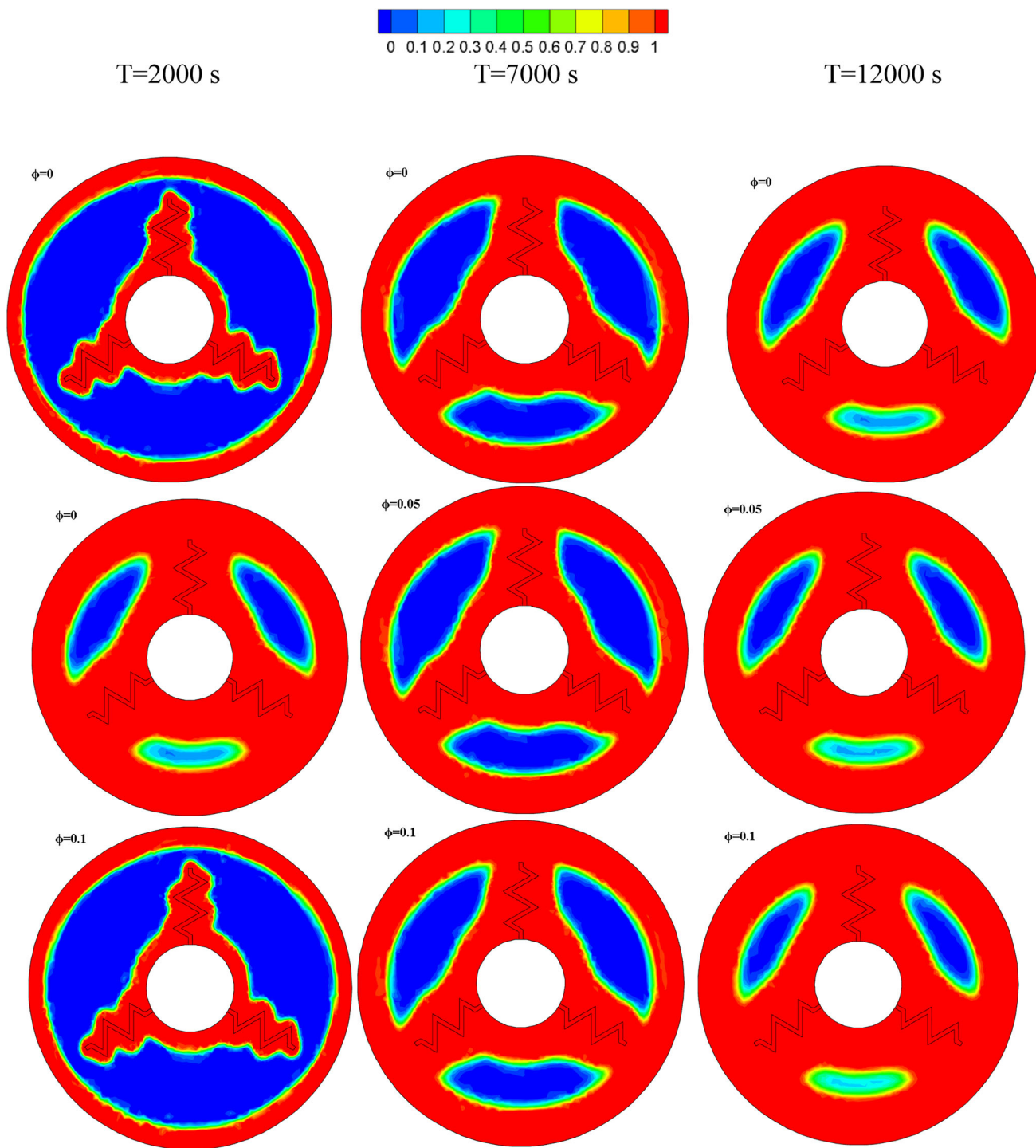
Figure 9. Solid fraction contour in different volume fractions of nanoparticles.

two cases without fins and the enclosure, including fins at different times, is depicted in figure 7. The figure shows the rate at which the liquid PCM transmits its energy to the cold fluid moving through the inner and outer tubes. This graph also shows that the total energy for both states declines with increasing time. Notably, times longer than 20,000 s exhibit minimal variation in the total energy since full solidification occurs during these intervals. Besides, the casing without fins consumes more energy than an enclosure with fins. The graphic shows that the lowest total energy quantity equals the system's maximum energy discharge capability. Figure 8 elucidates the solid fraction for two separate scenarios analysed in this section. The solidification rate
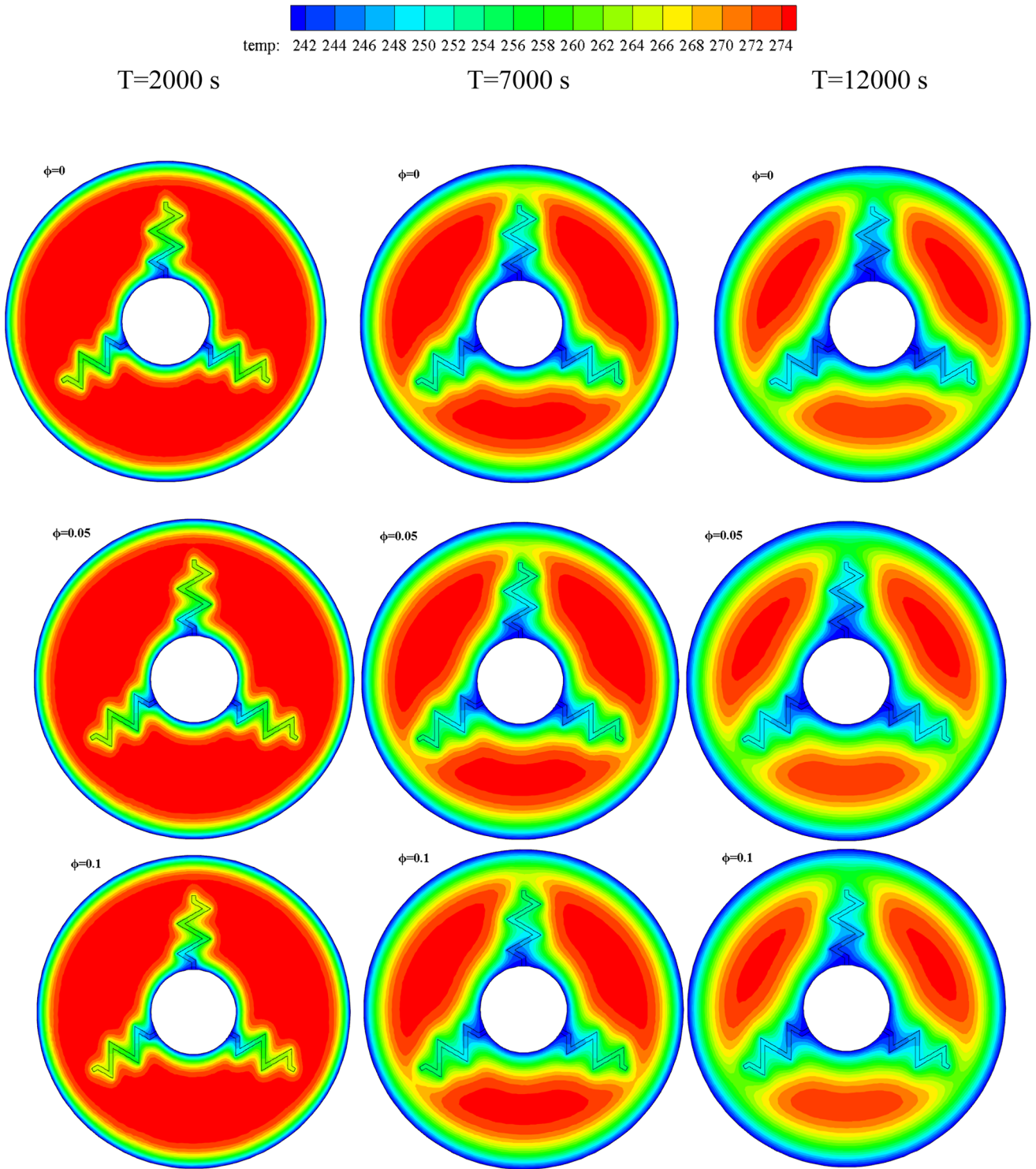
temp: 242 244 246 248 250 252 254 256 258 260 262 264 266 268 270 272 274

T=2000 s   T=7000 s   T=12000 s

Figure 10. Temperature contour in different volume fractions of nanoparticles.

can be determined from the slope of this graph. It is evident from the figure that the freezing rate is greater for the finned chamber than the standard chamber. Also, the time needed to achieve complete solidification is shorter for the chamber with fins than for the chamber without fins. The finned chamber reaches complete solidification in approximately 18,000 s, whereas it takes roughly 22,000 s for the standard chamber to attain full solidification after the commencement of the process. As a result, it can be inferred that the incorporation of fins
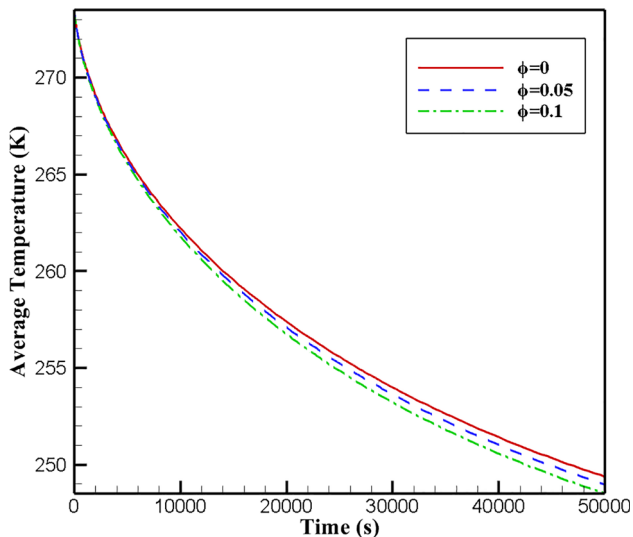
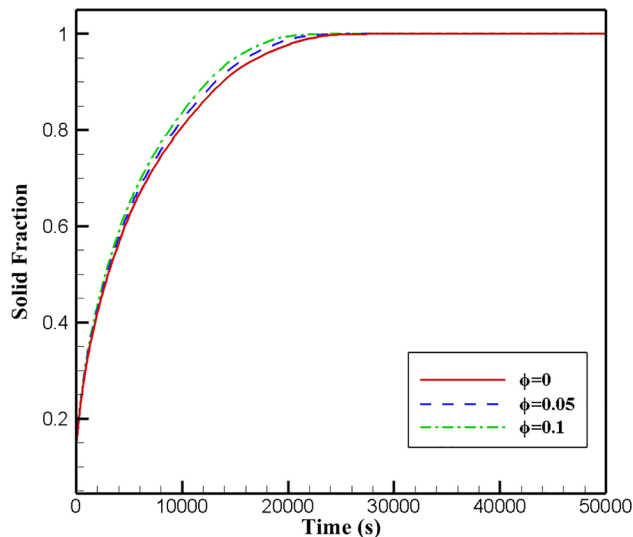**Figure 11.** Effect of the volume fraction of the nanoparticles on average temperature.

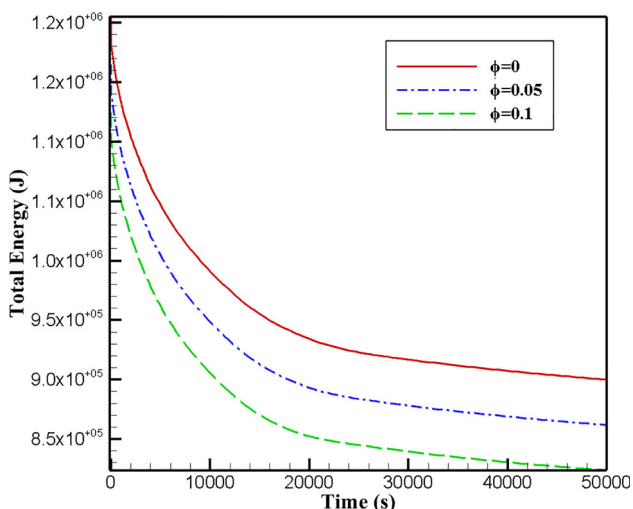**Figure 13.** Effect of volume fraction of the nanoparticles on the solid fraction.

Figure 12. Effect of the volume fraction of the nanoparticles on total energy.

enhances the solidification rate and diminishes the time required to achieve complete solidification.

4.2 *Different concentrations of HNEPCM evaluation*

In this section, the concentration parameter of HNEPCM is investigated. For this purpose, different concentrations (i.e., 0, 0.05 and 0.1) were considered. Also, the value of the radiation parameter is 0.5 and the shape factor of nanoparticles is 5.7. Figure 9 presents the solid fraction contour of the finned chamber at different times and various concentrations of HNEPCM. It is noteworthy that this contour is presented at various time

intervals, namely 2000, 7000 and 12,000 s. The findings indicate that the solid fraction of the PCM has increased over time. Additionally, the coefficient of thermal conductivity of the PCM rises together with the volume fraction of nanoparticles, speeding up the chamber's solidification process. Figure 10 elucidates the temperature distribution in the chamber with fins for various concentrations of HNEPCM. The findings indicate that the regions close to the cooling fluid exhibit lower temperatures in the PCM near both the inner and outer chamber walls compared to other areas within the chamber. Additionally, as time goes on, the temperature declines in different chamber areas. The PCM temperature is reduced by raising the nanoparticles' volume fraction and the conductive heat transfer coefficient. Figure 11 depicts the temperature distribution for HNEPCM's different concentrations. As can be seen, the average temperature of the PCM declines as time prolongs. Furthermore, the temperature variation is greater when the concentration is 0.05 than for other concentrations. Hence, a rise in the hybrid nanoparticle concentration results in more favourable outcomes.

Figure 12 presents the total energy for different concentrations. It can be concluded that total energy value indirectly relates to concentration. The findings indicate that the overall energy drops when the concentration of the hybrid nanoparticles rises. In other words, the system discharger process is improved. Figure 13 indicates the solid fraction for various concentrations at different time intervals. The conductive heat transfer coefficient rises together with the concentration of hybrid nanoparticles. As shown in the graph, an increase in HNEPCM
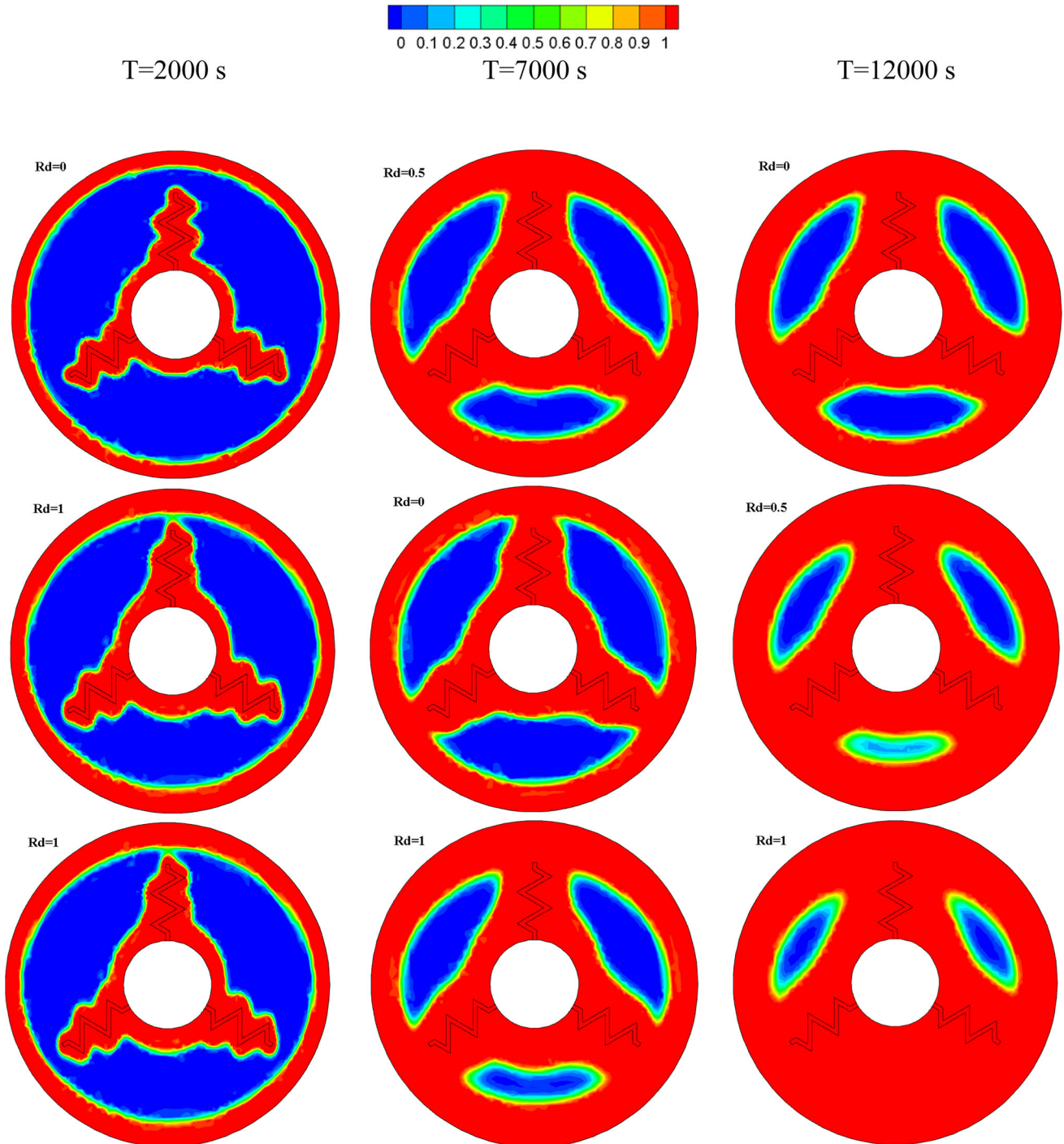
Figure 14. Solid fraction contour for different thermal radiation parameters.

concentration decreases the time required to complete the solidification.

4.3 *Investigation on the impact of radiation parameter*

This section provides the results for the effect of the radiation parameter. To this end, various values of the radiation parameter, including 0, 0.5 and 1, were examined. Also, the volume fraction of hybrid nanoparticles is 0.05 and the shape factor of the nanoparticles is 5.7. Figure 14 shows the solid fraction contour for different radiation parameters. As can be seen, by increasing the radiation parameter, a higher solid fraction can be obtained. The explanation is that with an increase in the radiation pramater, the thermal penetration depth
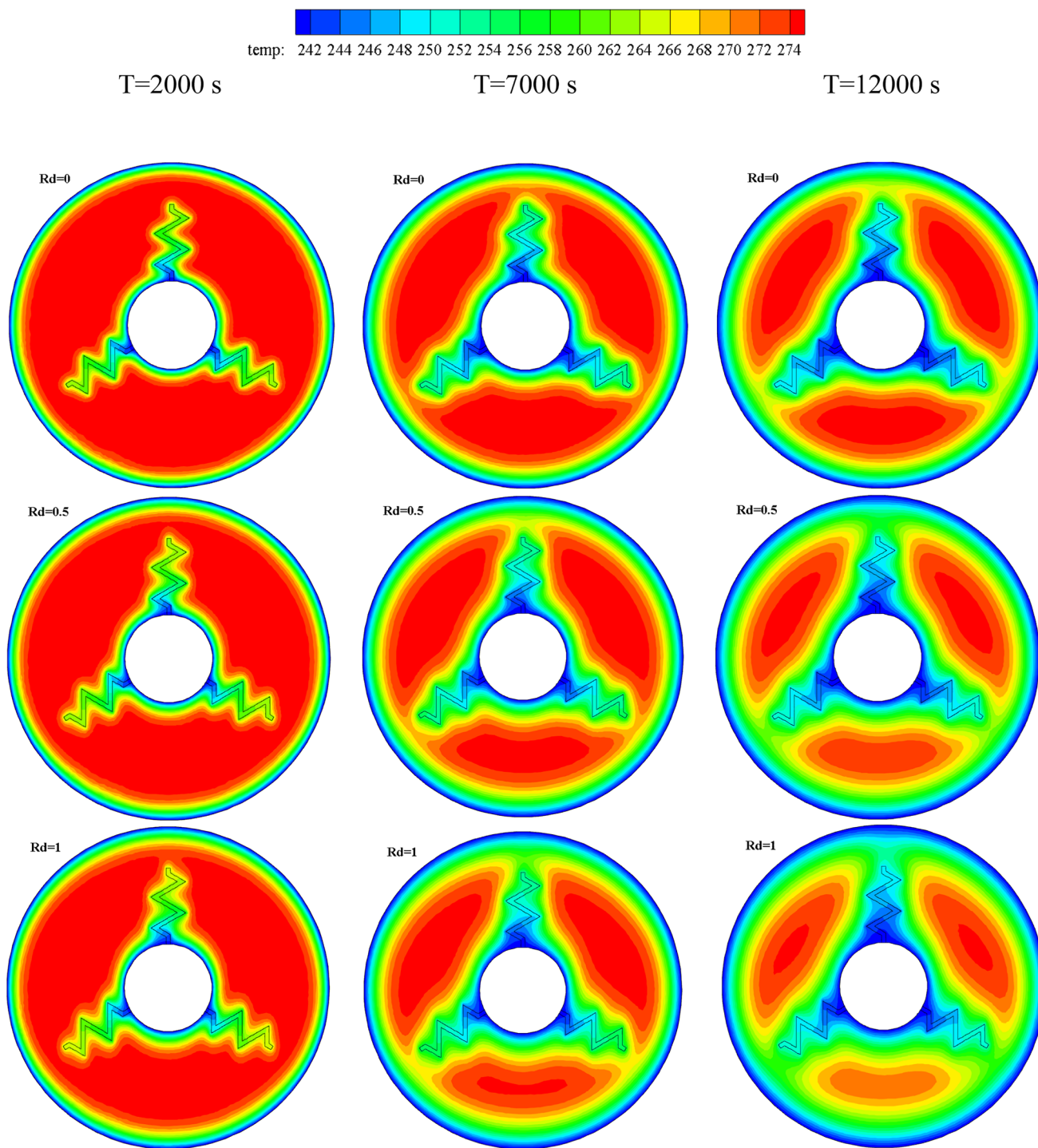
temp: 242 244 246 248 250 252 254 256 258 260 262 264 266 268 270 272 274

T=2000 s   T=7000 s   T=12000 s

Figure 15. Temperature contour in different values of thermal radiation parameter.

increases and faster completion of the solidification process is achieved. Figure 15 depicts the temperature contour of the finned chamber for different values of the radiation parameter. At 2000 s, the temperature around the fin is almost constant. As time increases, a uniform temperature distribution is created near the walls, indicating an increase in heat transfer. Also, with the rise in the radiation parameter, the temperature difference grows, thereby improving the heat transfer properties. The effect of the radiation parameter on the average temperature of the changing materials is demonstrated in figure 16.

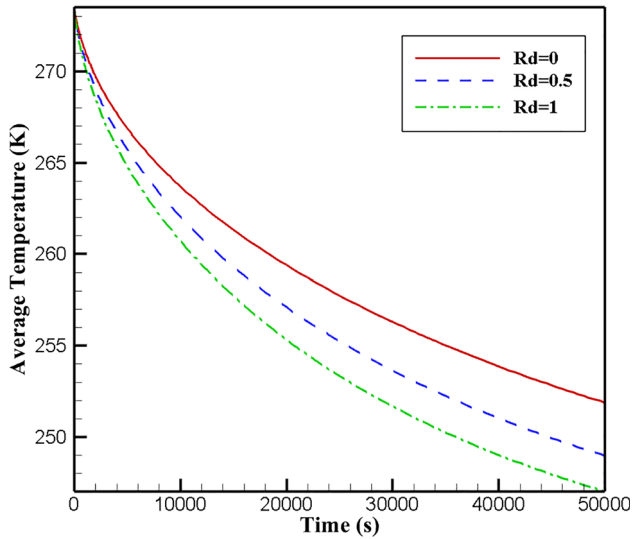As can be seen, the radiation parameter and the average temperature of the PCM are indirectly related to each

Figure 16. Effect of thermal radiation on the average temperature of the changing materials.
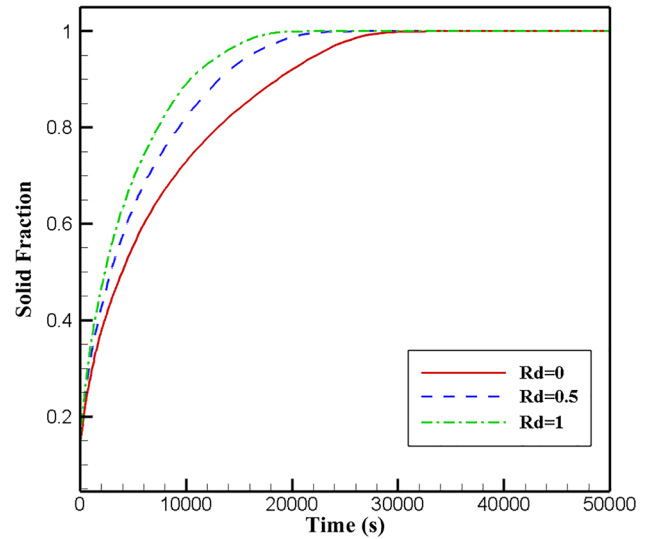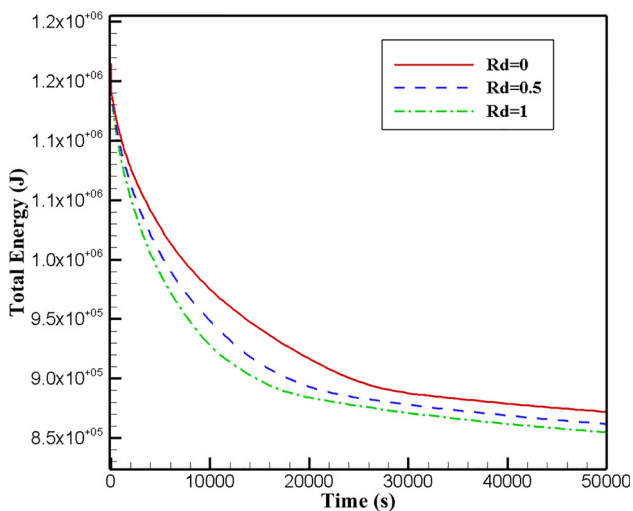

Figure 17. Effect of thermal radiation on total energy.

Figure 18. Effect of thermal radiation on the solid fraction.

4.4 *Evaluation of HNEPCM shape factor*

The impact of the nanoparticle shape factor is examined in this section. In this context, several shapes of nanoparticles (i.e., 3, 5.7 and 16.1) are studied. Here, the total volume fraction of the nanoparticles is 0.05 and the radiation parameter value is 0.5. Figures 19 and 20 depict the contour of the solid fraction for different shapes of HNEPCM at different times and the temperature contour of the finned chamber for different shape factors, respectively. The thermal conductivity of the hybrid nanoparticles is directly correlated with the shape factor. As a result, the thermal conductivity of the PCM increases, thereby enhancing the solidification rate in the chamber. Due to the proximity of the cooling fluid, the PCM near the inner and outer walls of the chamber experiences temperatures lower than other areas of the chamber. The diagram presented in figure 21 demonstrates how the average PCM temperature is affected by the shape parameters of the nanoparticles. A shape factor of 3 for the nanoparticles leads to a mean temperature higher than other shapes. In addition, the temperature difference of the PCMs for a shape factor of 16.1 is higher than other shapes. The effects of different HNEPCM shapes on the total energy are demonstrated in figure 22. Shape factors of the hybrid nanoparticles can be increased to optimise heat transfer and lower the overall energy level of the system, thereby enhancing the discharge rate. Figure 23 presents the effect of the shape factor of hybrid nanoparticles on the solid fraction. The time required to obtain 100% solidification declines by incrementing the shape factor of the nanoparticles. Furthermore, when the form factor increases, the average PCM temperature is reduced, incrementing the quantity
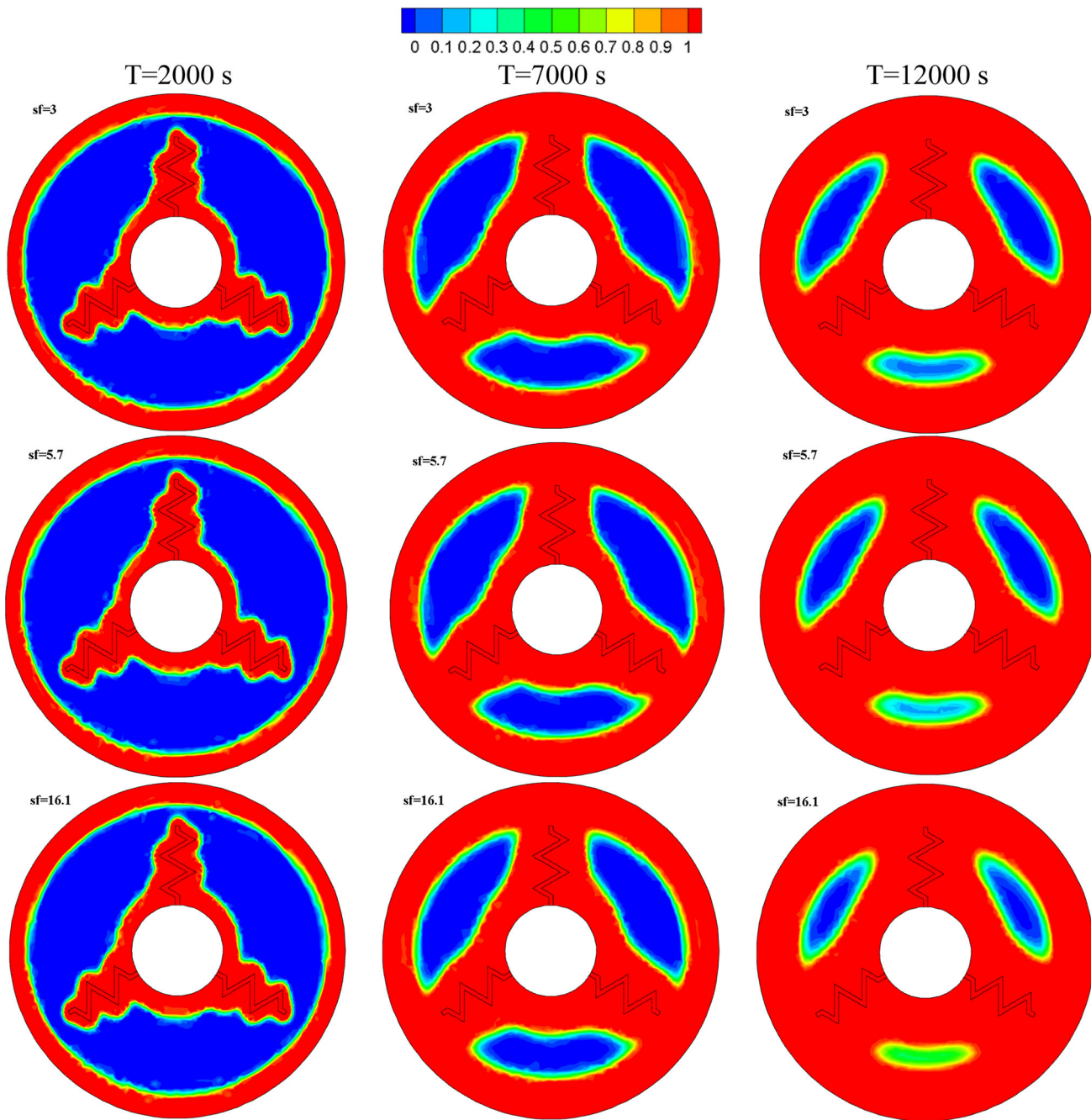
other. Notably, as the radiation parameter increases, the temperature difference rises. The slope of the graph line is higher in the beginning because the PCM and cooling fluid have a considerable temperature difference.

Figure 17 shows the impact of the radiation parameter on the total energy. This figure shows that the system's overall energy reduces when the radiation parameter increases. In other words, the system's discharger process is reinforced by raising the radiation parameter. As elucidated in figure 18, by increasing the radiation parameter, it takes less time to reach solidification. The solid fraction of the PCM also increases by increasing the radiation parameter. Accordingly, the solidification rate of the chamber rises when the radiation parameter is increased.

Figure 19. Contours of the solid fraction for different shapes of the nanoparticles.

of solid fraction. In other words, the solidification rate increases as the shape factor of the composite nanoparticles increases.

5. Conclusion

This study investigated how the acceleration of PCM solidification within a triplex LHTES chamber is influenced by hybrid nanoparticles, shape factor, extended surfaces and thermal radiation parameters (figure 23). The key findings are outlined as follows:

- The addition of fins strengthens the conductive heat transfer mechanism. Also, it increases the penetration of heat into the inner part of the chamber, thus enhancing the rate of solidification in the chamber.
- With the increased volume concentration of nanoparticles, the coefficient of thermal conductivity of the PCM also increases, resulting in a reduction in
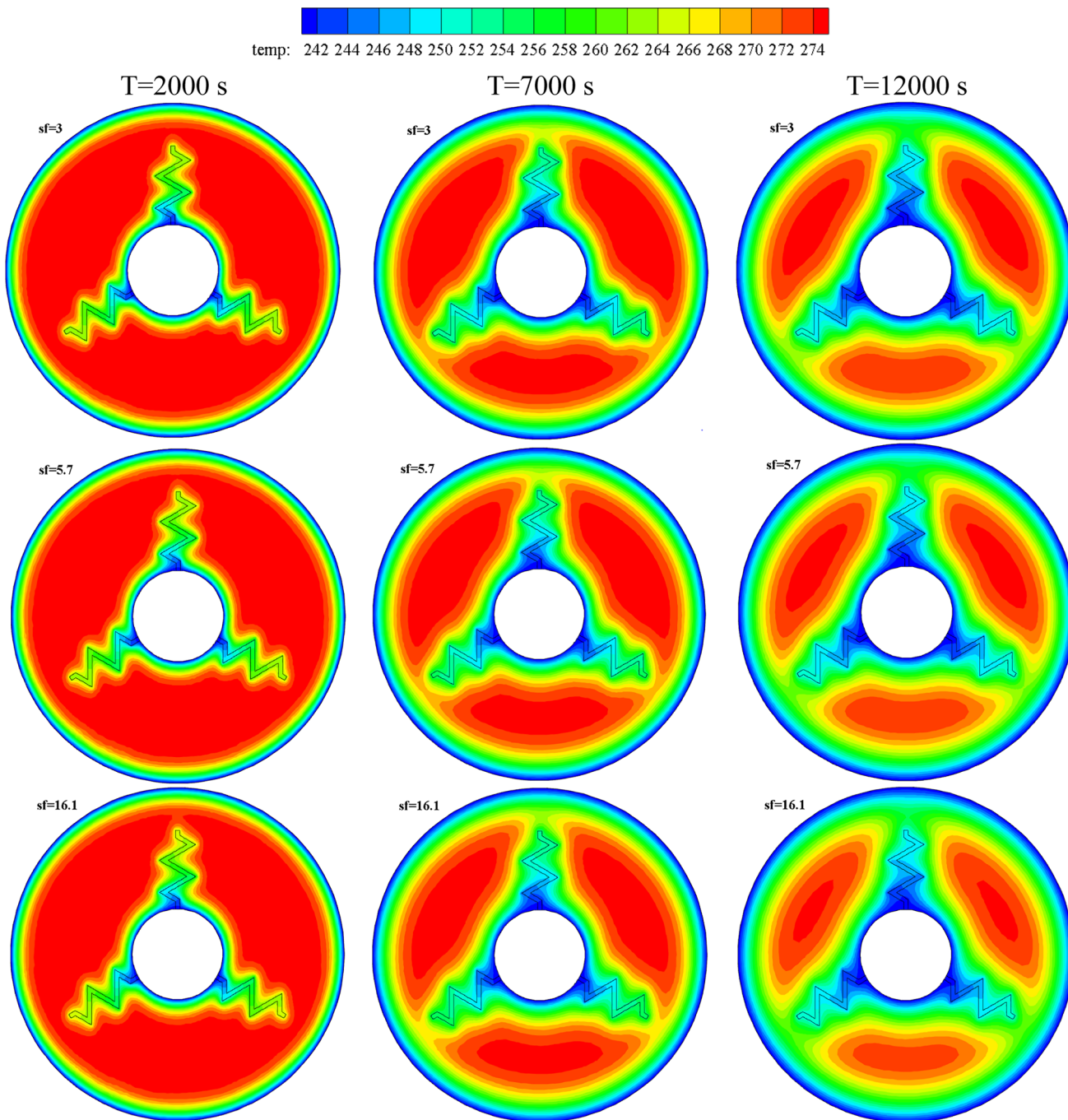
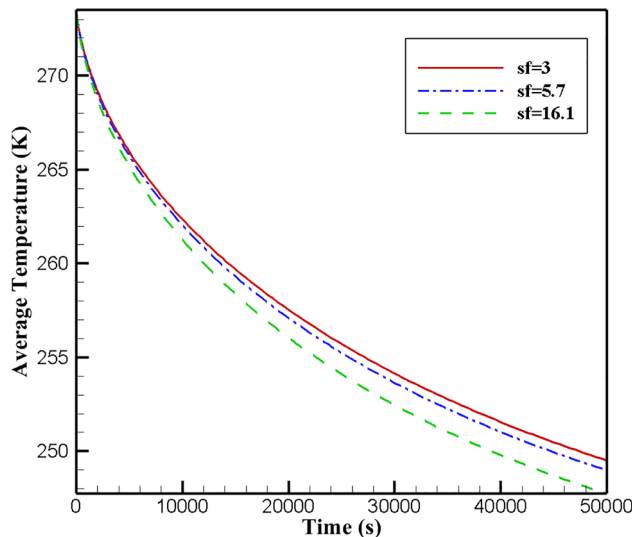**Figure 20.** Contours of the temperature for different shapes of the nanoparticles.

Figure 21. Effect of shape parameters of the nanoparticles on average temperature.
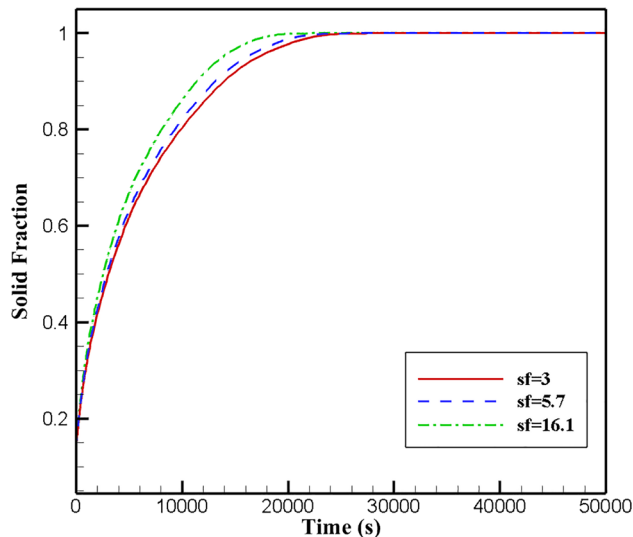

Figure 23. Effect of shape parameters of the nanoparticles on solid fraction.
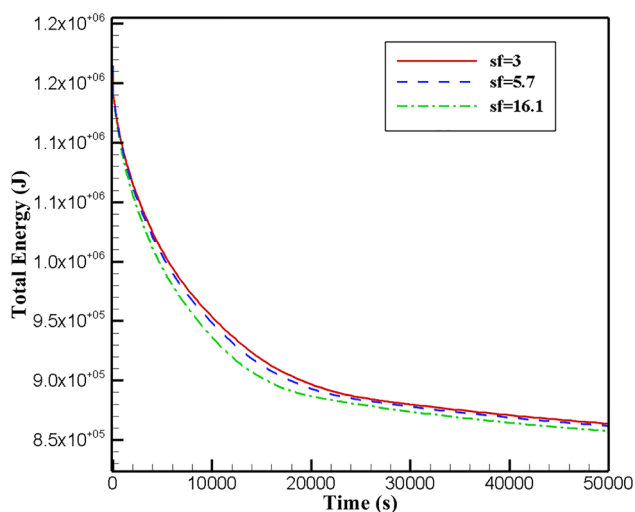

Figure 22. Effect of shape parameters of the nanoparticles on the total energy.

temperature and an increase in the solidification rate of the chamber.

- The amount of energy of the whole system decreases with the increased concentration of hybrid nanoparticles. In other words, the system discharger process is improved.
- As the radiation parameter increases, the thermal penetration depth increases, leading to the faster completion of the solidification process.
- The total energy of the system decreases by increasing the radiation parameter. In other words, the discharger process of the system is improved by increasing the radiation parameter.
- Rising the shape factor of hybrid nanoparticles affects the thermal conductivity directly. Ultimately,

it increases the thermal conductivity of the PCM and, thus, increases the solidification rate in the chamber.

References

[1] C Y Zhao, W Lu and Y Tian, *Sol. Energy* **84**(**8**), 1402 (2010)
[2] M Rostamizadeh, M Khanlarkhani and S M Sadrameli, *Energy Build.* **49**, 419 (2012)
[3] R Moradi, A Kianifar and S Wongwises, *Exp. Therm. Fluid Sci.* **89**, 41 (2017)
[4] P Saikia, A S Azad and D Rakshit, *Int. J. Therm. Sci.* **126**, 105 (2018)
[5] M Faghani, M J Hosseini and R Bahrampoury, *Alex. Eng. J.* **57**(**2**), 577 (2018)
[6] W Lin, W Zhang, Z Ling, X Fang and Z Zhang, *Appl. Therm. Eng.* **178**, 115630 (2020)
[7] A Sciacovelli, F Gagliardi and V Verda, *Appl. Energy* **137**, 707 (2015)
[8] M M Joybari, F Haghighat, S Seddegh and A A Al-Abidi, *Energy Convers. Manag.* **152**, 136 (2017)
[9] S Liu, H Peng, Z Hu, X Ling and J Huang, *Int. J. Heat Mass Transf.* **138**, 667 (2019)
[10] J R Patel and M K Rathod, *Heat Transf. – Asian Res.* **48**(**2**), 483 (2019)
[11] M Kirincic, A Trp and K Lenic, *J. Energy Storage* **42**, 103085 (2021)
[12] M S Shafiq, M M Khan and M Irfan, *Case Stud. Therm. Eng.* **27**, 101339 (2021)
[13] X Yang, F Xu, X Wang, J Guo and M J Li, *Energy Built Environ.* **4**, 64 (2023)
[14] S F Hosseinizadeh, A R Darzi and F L Tan, *Int. J. Therm. Sci.* **51**, 77 (2012)
[15] S Y Wu, H Wang, S Xiao and D S Zhu, *J. Therm. Anal. Calorim.* **110**(**3**), 1127 (2012)

[16] M Sheikholeslami and A Ghasemi, *Int. J. Heat Mass Transf.* **123**, 418 (2018)

[17] Z Khan, Z A Khan and P Sewell, *Int. J. Heat Mass Transf.* **144**, 118619 (2019)

[18] A Yadav and M K Shivhare, Nanoparticle-enhanced PCM for solar thermal energy storage, in: *IEEE Advances in Science and Engineering Technology International Conferences (ASET)* pp. 1–3 (2020)

[19] S M H Zadeh, S A M Mehryan, M Ghalambaz, M Ghodrat, J Young and A Chamkha, *Energy* **213**, 118761 (2020)

[20] M E Moghaddam, M H S Abandani, K Hosseinzadeh, M B Shafii and D D Ganji, *Theor. Appl. Mech. Lett.* **12**(**2**), 100332 (2022)

[21] K Hosseinzadeh, A Asadi, A R Mogharrebi, B Jafari, M R Hasani and D D Ganji, *Alex. Eng. J.* **60**(**1**), 1967 (2021)

[22] K Hosseinzadeh, E Montazer, M B Shafii and A R D Ganji, *J. Energy Storage* **34**, 102177 (2021)

[23] K Hosseinzadeh, S Faghiri, S Akbari, J R Kermani, B Jafari and M B Shafii, *Int. J. Thermofluids* **20**, 100443 (2023)

[24] A Najafpour, K Hosseinzadeh, S Akbari, M Mahboobtosi, A A Ranjbar and D D Ganji, *Chem. Eng. Processing-Process Intensification* **194**, 109567 (2023)

[25] M Mohammadi, K Hosseinzadeh and D D Ganji, Numerical analysis on the impact of axial grooves on vortex cooling behavior in gas turbine blade's leading edge, *Proceedings of the Institution of Mechanical Engineers, Part E: Journal of Process Mechanical Engineering*, 09544089231163113 (2023)

[26] M R Mardani, D D Ganji and K H Hosseinzadeh, *J. Mol. Liq.* **346**, 117111 (2022)

[27] A Najafpour, K Hosseinzadeh, J R Kermani, A A Ranjbar and D D Ganji, *J. Mol. Liq.* **393**, 123616 (2023)

[28] N Alipour, B Jafari and K Hosseinzadeh, *Heliyon* **9**, e22257 (2023)

[29] M Mahboobtosi, K Hosseinzadeh and D D Ganji, *Int. J. Thermofluids* **20**, 100507 (2023)

[30] M R Zangooee, K Hosseinzadeh and D D Ganji, *Case Stud. Therm. Eng.* **50**, 103398 (2023)

[31] K Hosseinzadeh, M Roshani, M A Attar, D D Ganji and M B Shafii, *Heliyon* **9**(**9**), e20193 (2023)

[32] M R Moradi, K Hosseinzadeh, A Hasibi and D Domiri Ganji, https://doi.org/10.1080/10407790.2023.2241632 (2023)

[33] K Hosseinzadeh, S Akbari, S Faghiri and M B Shafii, *Int. J. Thermofluids* **18**, 100337 (2023)

[34] K A R Ismail, C L F Alves and M S Modesto, *Appl. Therm. Eng.* **21**(**1**), 53 (2001)